Ultrabroadband Tuning and Fine Structure of Emission Spectra in Lanthanide Er-Doped ZnSe Nanosheets for Display and Temperature Sensing

Yuan Liu[a], Gongxun Bai[a,*] Yongxin Lyu[b], Youjie Hua[a,c], Renguang Ye[a], Junjie Zhang[c], Liang Chen[c], Shiqing Xu[a,*], and Jianhua Hao [b,*]

[a] *Institute of Optoelectronic Materials and Devices, China Jiliang University, Hangzhou 310018, People's Republic of China*

[b] *Department of Applied Physics, The Hong Kong Polytechnic University, Hong Kong, People's Republic of China*

[c] *College of Optics and Electronic Technology, China Jiliang University, Hangzhou 310018, People's Republic of China*

ABSTRACT:

Realizing multi-colored luminescence in two-dimensional (2D) nanomaterials would afford potential for a range of next-generation nanoscale optoelectronic devices. Moreover, combining fine structured spectral line emission and detection may further enrich the studies and applications of functional nanomaterials. Herein, a lanthanide doping strategy has been utilized for the synthesis of 2D $ZnSe:Er^{3+}$ nanosheets to achieve fine-structured, multi-color luminescence spectra. Simultaneous upconversion and down-conversion emission is realized, which can cover an ultrabroadband optical range, from ultra-violet through visible to the near-infrared region. By investigating the low-temperature fine structure of emission spectra at 4 K, we have observed an abundance of sublevel electronic energy transitions, elucidating the electronic structure of Er^{3+} ions in the 2D ZnSe nanosheet. As the temperature is varied, these nanosheets exhibit tunable multi-colored luminescence under 980 and 365 nm excitation. Utilizing the distinct sublevel transitions of Er^{3+} ions, the developed 2D $ZnSe:Er^{3+}$ optical temperature sensor shows high absolute (15.23% K^{-1}) and relative sensitivity (8.61% K^{-1}), which is superior to conventional Er^{3+} activated upconversion luminescent nanothermometers. These findings imply that Er^{3+} doped ZnSe nanomaterials with direct and wide bandgap have the potential for applications in the future low-dimensional photonic and sensing devices at the 2D limit.

KEYWORDS: lanthanide phosphors, 2D nanosheets, ZnSe, multi-color, temperature sensing

Nanomaterials with two-dimensional (2D) forms have attracted significant research interest due to their notable optoelectronic properties.[1-3] Generally, 2D nanomaterials have lateral dimensions larger than 100 nm, but less than 5 nm in thickness.[4] Owing to their interesting characteristics, 2D nanomaterials research has spanned a diverse range of fields, such as electronic devices, photonics, and sustainable energy.[5-8] Among them, the photonic performance of 2D materials is crucial for many devices that could play an important role in the next-generation photonic technology.[9,10] Hence, the photoluminescence (PL) features of 2D nanomaterials have received intense attention.[11,12] The PL performance of 2D nanomaterials is determined by the radiative transitions of excited electrons in diverse classes of 2D compounds, such as transition metal dichalcogenides (TMDs) and III−VI group semiconductors.[13-15] To date, the tuning of luminescence is mainly achieved by selecting 2D semiconductors with particular bandgap energies, as governed by the particular excitonic characteristics, as well as the number of layers in the 2D flakes. Attempts have been made to continuously tune the PL properties of 2D nanomaterials. For instance, Li *et al*. investigated the effect of layer number on the PL properties of 2D WS_2 nanosheets.[16] Hu *et al.* observed fascinating PL phenomena by twisting the stack angle of α-MoO_3 bilayers.[17] However, these methods can only achieve the wavelength tuning over a limited range. Additionally, doping strategies are increasingly being used to modify the PL properties of 2D nanomaterials. Typically, transition metal manganese was introduced into MoS_2 host to tune PL emission.[18] The implantation of noble metal gold into 2D nanomaterials has been performed for luminescent modification.[19] Likewise, our group demonstrated near-infrared (NIR) emission at 800 and 1550 nm of 2D MoS_2 nanosheets *via* introducing rare-earth (RE) ions as dopants.[20] Whereas, the band gap of conventional TMDs (MoS_2, WS_2, WSe_2 *etc*.) is relatively narrow, which only permits NIR emissions of RE ions.

Despite these efforts, multi-colored tuning with fine structure of optical spectra in 2D nanomaterials has not been explored. It is of great significance for investigating the fine structure of spectral lines for both fundamental research and multi-colored luminescence devices such as ultrathin displays and optical sensors at the 2D limit.

Theoretically, RE doped 2D nanomaterials with wide bandgap could generate abundant emissions. Unfortunately, there are few reports on the RE doped 2D nanomaterials with multi-colored luminescence. It should be noted that the ZnSe is a direct band gap semiconductor both in monolayer and multilayer form whilst also possessing a wide band gap energy range (2.7-3.5 eV).[21] Different from some typical 2D nanomaterials, the ZnSe semiconductor possesses high crystal purity and exhibits a transparent yellow color which more weakly absorbs visible light. Earlier studies have demonstrated photocatalysis applications in single layered ZnSe nanosheets,[21] implying that 2D ZnSe nanosheets with good photonic properties should provide a favorable matrix for RE ions.

Moreover, nanoscale sensing has drawn attention from researchers because of advantages in both size and performance. Among optical sensing technologies, thermal sensors have potential for a broad range of applications due to their fast response and non-contact nature.[22-25] Owing to the thermally coupled energy levels, Er ions are widely applied in radiometric temperature sensing. For example, Yb/Er/Cr triply doped oxyfluoride glass has been employed for optical thermometry,[26] while core-shell $NaYF_4$:Yb,Er@$NaYF_4$ nanoparticles have been used for temperature sensing.[27] However, further study is desired to achieve high thermometric sensitivity owing to the overlap of emission bands and the host effect on the Er-actived ions which limits the application potential. It is essential to explore whether this problem could be solved through adopting 2D nanomaterials as a sensing platform; combining RE ions and 2D ZnSe semiconductors could see an improvement in photophysical characteristics and enhanced sensing performance.

Here, we have synthesized ZnSe nanosheets doped with lanthanide Er ions by a two-step method. We demonstrate tuning of multi-colored luminescence in these nanosheets. The 2D nanomaterials doped with Er can produce ultrabroadband optical emission ranging from ultra-violet (UV), visible with green, red, and yellow emissions to near-infrared (NIR) in a single compound. Further, we make use of the sub-level intensity ratio of Er ions emission to overcome the obstacle of overlapped emission-peaks and

realize high thermometric sensitivity, greatly broadening the range of potential applications for these materials.

RESULTS AND DISCUSSION
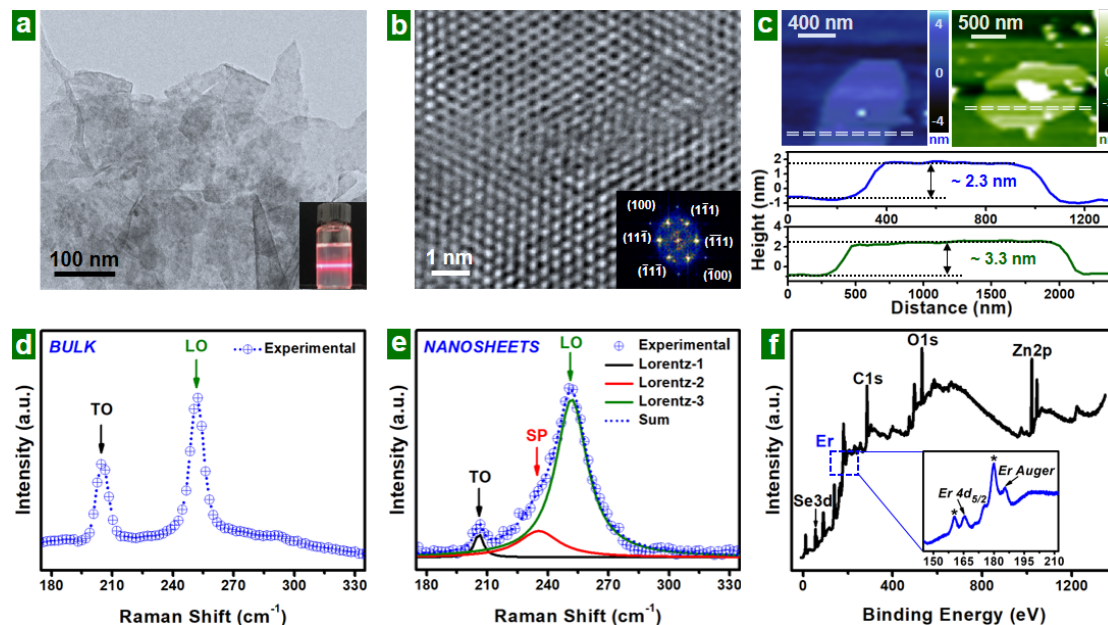
Figure 1. The morphology and structure of ZnSe:Er^{3+} nanosheets. (a) TEM image. Inset: the nanosheets suspension under laser irradiation. (b) HR-TEM image and the relevant diffraction spots using fast Fourier transform. (c) AFM images in various plane sizes and their corresponding height profiles. (d) Raman spectrum of bulk powders. (e) Raman spectrum of nanosheets and corresponding Lorentz deconvolution. (f) XPS spectrum of nanosheets.

Morphology and structure play an important role in the physical properties of nanomaterials. The X-ray diffraction (XRD) patterns of nanosheets and bulk match well with the standard card (PDF#37-1463, Figure S1). No secondary and hetero-phases of materials are obviously observable, which suggests that both ZnSe:Er^{3+} samples have a pure cubic structure with space group of F-43m (Table S1). It seems that the doping of Er^{3+} ions has little influence on the crystal structure of the ZnSe host. Moreover, the exfoliated nanosheets present a different face-preferred orientation from the bulk, which can be attributed to a lower surface energy of (110) lattice planes compared with the (100) or (111) facets.[21] According to previous research, the (110) facets are proved

to be cleavage planes of ZnSe (Figure S2).[28] Therefore, under certain forces, the bulk ZnSe could be cleaved along the (110) facets with relative ease. Transmission electron microscope (TEM) and high-resolution TEM (HR-TEM) were utilized to elucidate the morphology of as-prepared nanosheets. As shown in Figure 1a, the prepared nanosheets are ultrathin with lateral sizes of hundreds of nanometers. The inset illustrates that the nanosheets were dispersed in ethanol medium and exhibit a Tyndall effect. Figure S3 further shows that only the nanosheets dispersion possesses the Tyndall effect and the corresponding SEM images also display the different micro-morphology of bulk and nanosheets. It can be inferred that the primal ZnSe:Er^{3+} bulk was exfoliated into sheets form after ultrasonic and centrifuge processing. Figure 1b illustrates the HR-TEM pattern of fabricated nanosheets. After fast Fourier transform analysis, the observed lattice face is determined to be (111), which further verifies the (110) preferred orientation of nanosheets (Figure S1, S4). In addition, as shown in Figure S5, the scanning TEM (STEM) with spherical aberration correction was utilized to study the different microstructures of the ZnSe:Er^{3+} powder and nanosheets. Atomic force microscopy (AFM) was carried out for measuring the thickness and plane size. Several nanosheets with flat surfaces and diverse size were observed clearly in Figure 1c. The plane size is determined to be hundreds of nanometers and the corresponding height profiles of the nanosheets are around 2.3 and 3.3 nm. According to a previous report,[21] the thickness of monolayer and bilayer ZnSe nanosheets is determined to be 0.91 and 2.5 nm, respectively. It can be deduced that the as-prepared nanosheets are approximately 2~3 layers. Hence, these results suggest that 2D ZnSe:Er^{3+} nanosheets with few layers have been fabricated.

Raman spectroscopy was employed for studying vibration modes of ZnSe:Er^{3+} nanosheets. As shown in Figure 1d, two scattering peaks were clearly observed at 205.4 and 251.8 cm^{-1} in the ZnSe:Er^{3+} bulk, which are originated from transverse optical (TO) and longitudinal optical (LO) phonon modes, respectively.[29] Figure 1e illustrates the Raman spectrum of the fabricated ZnSe:Er^{3+} nanosheets. After Lorentz deconvolution, three peaks were acquired at 205.7, 235.3, and 251.6 cm^{-1}. The first and third peaks are attributed to TO and LO modes, respectively. According to previous research,[30] the

second Raman peak is attributed to the surface phonon (SP) mode. Comparing the two sets of Raman spectra, a Raman peak regarded as an SP mode arises from bulk to nanosheets of ZnSe:Er^{3+}. In general, the SP mode is hard to observe because of its low Raman intensity in the bulk form. As the bulk is converted into nanosheets, this vibration mode is gradually disclosed. This observation can be attributed to the quantum size effect, which increases the ratio of surface to volume and then enhances the intensity of the SP mode.

The composition of the fabricated nanosheets was investigated via X-ray photoelectron spectroscopy (XPS) detection. As shown in Figure 1f, the spectrum illustrates the existence of Zn, Se and Er elements in nanosheets. The C element originates from the allochthonous carbon, and the O element comes from the oxygen adsorbed on the sample surface. The peaks at 1021.8 and 1044.7 eV originate from the Zn 2p3 and Zn 2p1 doublets, respectively, while the peak located at 54.5 eV originates from the Se 3d binding energy.[31] The two peaks at 165.6 and 185.5 eV originate from the Er 4d$_{5/2}$ and Er Auger signals.[20] Moreover, the binding energy peaks of ErF$_3$ are not detectable here. As shown in Figure S6, the elemental distribution of the prepared samples was analyzed by energy dispersive X-ray spectroscopy (EDS), which further reveals the presence of Er element in the ZnSe host. The XPS results combined with the above experimental data suggest that Er ions have been introduced into the ZnSe nanosheets matrix without secondary and hetero-phases forming.
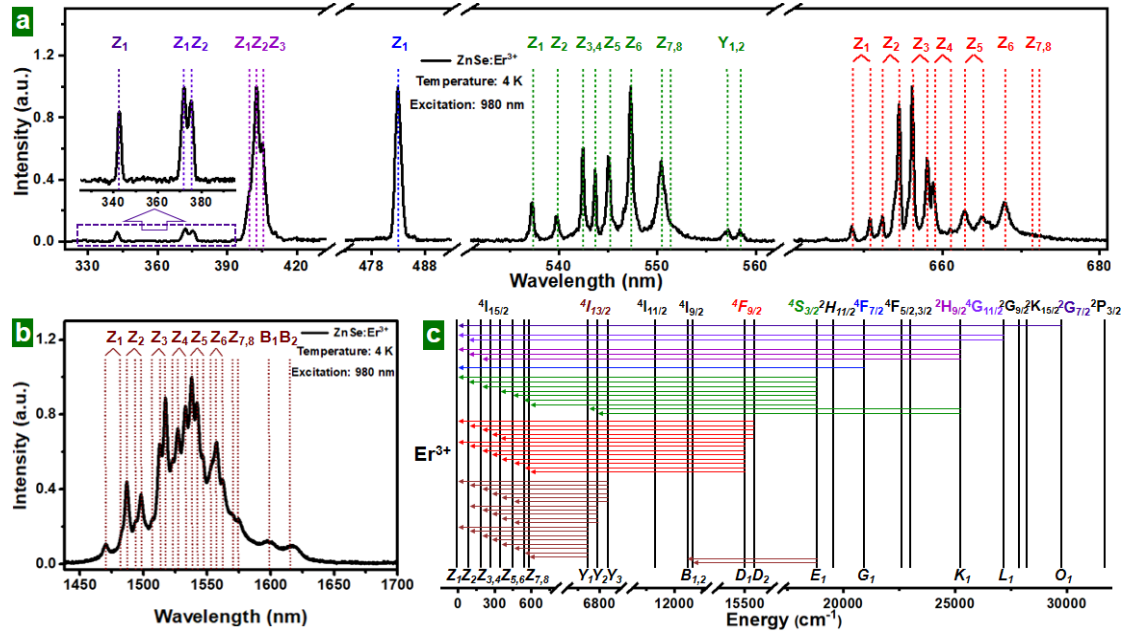
Figure 2. The 4 K fine emission spectra of ZnSe:Er^{3+} nanosheets under 980 nm excitation. (a) Upconversion emission spectra of nanosheets from UV to visible range. (b) Down-conversion emission spectra of nanosheets at NIR range. (c) Energy levels of Er^{3+} in ZnSe nanosheets and corresponding CF transitions.

The luminescence properties of as-prepared ZnSe:Er^{3+} nanosheets are analyzed through PL spectra measurements. Figure S7 reveals the up- and down-conversion (UC and DC) luminescence spectra of as-prepared nanosheets under 980 nm excitation at room temperature (298 K). To avoid thermal broadening effects, fine emission spectra of ZnSe:Er^{3+} nanosheets are monitored at a low temperature of 4 K. As shown in Figure S8, the full width at half maximum (FWHM) of the emission peaks is smaller than 0.9 nm. Figure 2a and b show the UC and DC PL spectra of as-prepared nanosheets under 980 nm excitation at 4 K.

As shown in Figure 2a, the UC emissions are observed clearly covering the UV and visible areas. In the UV range, the peaks located at 342.6, 372.0, and 375.3 nm originate from the electronic transitions of O_1, L_1 to Z_1 and L_1 to Z_2 in Er^{3+} doped ZnSe nanosheets, respectively. Whereas, the luminescence of original ZnSe:Er^{3+} bulk can hardly be observed at the UV spectra range (Figure S9, S10). On the one hand, this may be due to the low UC probability of Er^{3+} at a short wavelength range. On the other hand,

we also attribute this result to a high free luminescence phenomenon for nanomaterials with 2D form. Typically, the PL property of RE ions is restricted by the band gap energy of the host materials, that is, the emission wavenumber of RE ions is normally smaller than that from the host. This can be mainly attributed to that the photon energy (UV range) is absorbed by host materials with bulk form for lattice vibrations working. But after exfoliation into 2D form, absorption will be greatly weakened for single or few layers nanosheets as illustrated in Figure S11. The absorption spectra of nanosheets are shown in Figure S12. We deduce that the quantum confinement, saturated absorption and edge effects in the nanosheets induce weakened absorption and blue-shift the bandgap.[11,32] There are violet, blue, green, and red emission bands in the visible range, corresponding to the emission peaks at 402.8, 482.9, 547.3, and 656.1 nm, respectively. They are originated from the $K_1 \rightarrow Z_2$, $G_1 \rightarrow Z_1$, $E_1 \rightarrow Z_6$, and $D_2 \rightarrow Z_3$ transitions in Er^{3+} doped ZnSe nanosheets, respectively. Figure 2b illustrates the 4 K DC emission spectra of ZnSe:Er^{3+} nanosheets under 980 nm excitation. The NIR emission bands with the strongest peak at 1537.8 nm can be distinctly observed, which corresponds to the transition of Y_3 to Z_5 in Er^{3+} doped ZnSe nanosheets. Corresponding to the above results of UC and DC emission spectra, the crystal field (CF) energy level diagram of Er^{3+} in ZnSe nanosheets is shown schematically in Figure 2c. The ground state of $^4I_{15/2}$ has non-degenerated to eight CF levels, including Z_1, Z_2, Z_3, Z_4, Z_5, Z_6, Z_7, and Z_8. The excited state levels are each split into several sublevels. For instance, the excited state $^4I_{13/2}$ splits into Y_1, Y_2, and Y_3 sublevels, resulting in the majority of NIR emission, while the $^4I_{9/2}$ splits into B_1 and B_2 sublevels for the remainder. For the red luminescence, two sublevels (D_1 and D_2) of the excited state $^4F_{9/2}$ are observed. The rest of excited states, such as $^4S_{3/2}$, $^4F_{7/2}$, $^2H_{9/2}$, $^4G_{11/2}$, and $^2G_{7/2}$ can be observed as a single CF level, corresponding with E_1, G_1, K_1, L_1, and O_1, respectively.

In addition, the full range of emission peaks and corresponding CF energy levels are further studied and labeled in Table S2 and S3. All of the emission peaks from UV to NIR range of Er^{3+} originate from these sublevel transitions. For the green emission, ten CF lines are observed with wavelengths of 537.3, 539.8, 542.6, 543.8, 545.2, 547.3, 550.5, 551.3, 557.2, and 558.6 nm, corresponding with the E_1 to Z_J (*J*=1-8) and K_1 to

$Y_{1,2}$ sublevel transitions. In regard to the thirteen red emission peaks, such as 648.5, 650.8, 652.4, 654.5, 656.1, 658.2, 659.2, 661.1, 662.9, 665.3, 668.0, 671.5, and 672.3 nm, they mainly originate from the $D_{1,2} \rightarrow Z_J$ sublevel transitions. Specifically, these transitions are determined to be $D_2 \rightarrow Z_{J'}$ (J'=1-5) and $D_1 \rightarrow Z_{J''}$ (J''=1-8) CF lines. Owing to the broader energy level of $^4I_{13/2}$, the total twenty-one NIR emissions are determined to be from 1469.9 to 1615.2 nm. These CF lines are originated from the Y_3 to Z_{J1} (J_1=1-6), Y_2 to Z_{J2} (J_2=2-6), Y_1 to Z_{J3} (J_3=1-8), and E_1 to $B_{1,2}$ sublevel transitions.
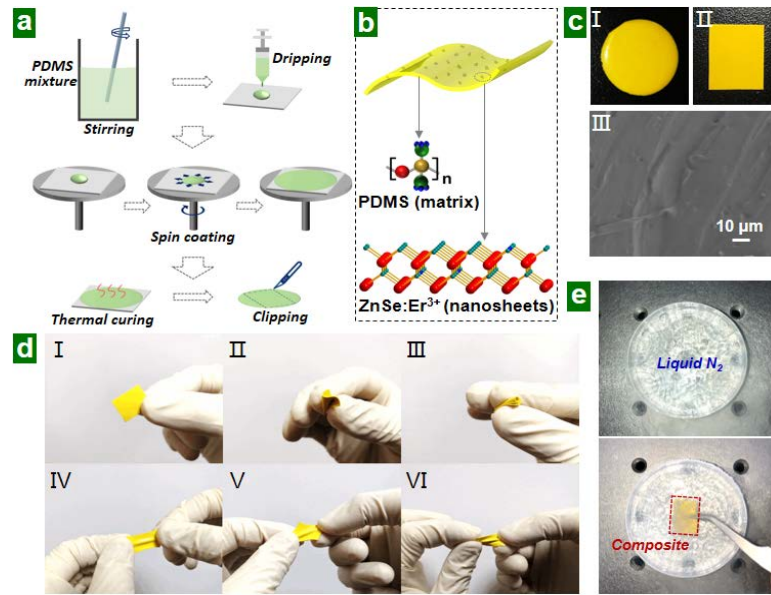
Figure 3. Flexible composite film consisting of ZnSe:Er^{3+} nanosheets and PDMS matrix. (a) Fabrication process of the composite film. (b) Schematic diagram of the composite film. (c) Top-view photos of the circle I) and rectangle II) composite film; the cross-section SEM image III). (d) The flexibility test of the composite film. (e) The composite film is immersed in liquid N_2.

Having obtained the fine structure of the spectral lines and demonstrated broad luminescence emission, we move forward to design and fabricate flexible 2D ZnSe:Er^{3+} optical devices. The stretchable composite films were fabricated by dispersing the ZnSe:Er^{3+} nanosheets into polydimethylsiloxane (PDMS) elastomers. PDMS possesses several advantages, such as flexibility, high-transparency, and frigostability suitable for flexible optoelectronics.[27] As shown

in Figure 3a, the process of composite fabrication consists of three steps. First, the PDMS colloid is mixed with the ZnSe:Er^{3+} nanosheets at a ratio of 1:3 in a beaker, and then the PDMS mixture is drop-cast onto a glass substrate by an injector. Secondly, the composite precursor is spread and thinned via spin-coating. The rotation speed of the spin coater is a vital parameter to adjust the uniformity and thickness of the composite film. A low rotation speed combined with repeated coating is beneficial to forming high-quality composite film. Thirdly, the PDMS mixture is thermally cured in a drying oven at 60 °C for 2 hr. The fabricated PDMS composite film was then clipped into shapes for further experiments. Figure 3b illustrates the schematic of the composite film consisting of ZnSe:Er^{3+} nanosheets and the PDMS matrix. The ZnSe:Er^{3+} nanosheets are distributed uniformly in the PDMS matrix to achieve desirable PL properties. The specific sample of the composite film is shown in Figure 3c. The prepared composite film appears yellow from the top-view images, attributed to the optical color of ZnSe. The cross-sectional SEM image further indicates the uniform distribution of the ZnSe:Er^{3+} nanosheets in PDMS matrix. To verify their flexibility, the fabricated composite films were subjected to different processes of bending, crimping, horizontal stretching, and diagonal stretching as shown in Figure 3d. The series of pictures demonstrate that the prepared composite film shows sufficient flexibility. In addition, the composite film also reveals good resistance to low temperature. As shown in Figure 3e, liquid N$_2$ at 77 K was poured into a transparent plastic petri dish. The fabricated composite film was submerged into the liquid N$_2$ with tweezers. After this treatment, the composite film still retains its flexible performance (Figure S13) at room temperature.
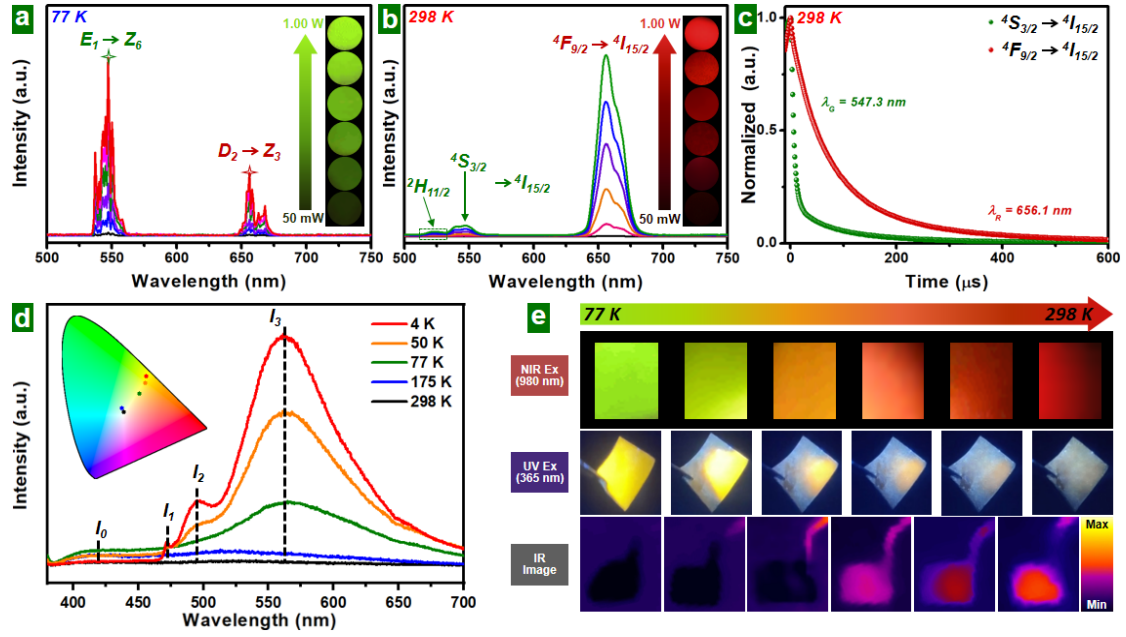
Figure 4. Multi-color PL spectra of the ZnSe:Er^{3+} composite film. (a) 77 K emission spectra at increasing power under 980 nm excitation. The inset shows the corresponding PL image. (b) Room-temperature power-dependent emission spectra pumped at 980 nm. The inset displays the relevant PL images. (c) Room-temperature decay curves of the green and red emission peaks under 980 nm excitation. (d) Emission spectra at different temperature under 365 nm excitation. Inset: the CIE chromaticity and corresponding color coordinates. (e) Temperature-dependent images of the composite film involving NIR excitation (top), UV irradiation (middle), and IR imaging.

The emission spectra of the ZnSe:Er^{3+} composite film under varying pump power and temperature were characterized to further elucidate the luminescent processes. As shown in Figure 4a, the emission intensities of green and red bands tend to strengthen when the pump power is increased. The insets further display the brightness variation as the power is increased from 50 mW to 1.00 W at 77 K. Figure 4b illustrates the change of emission spectra as the pump power increases at 298 K. Similarly, the emission intensity is enhanced, with correspondingly brighter luminescence as the incident power increases. On the other hand, the FWHM of the emission peaks are broadened compared with the 77 K spectra, largely due to the vibronic transition at room temperature. Typically, there are two energy transitions of green emission for Er^{3+}:

$^2H_{11/2} \rightarrow {}^4I_{15/2}$ and $^4S_{3/2} \rightarrow {}^4I_{15/2}$. However, it can be clearly observed that the emission intensity from $^2H_{11/2} \rightarrow {}^4I_{15/2}$ is particularly weak at room temperature, and hardly visible at 77 K, as shown in Figure 2 and 4a. This can be attributed to the phenomenon of phonon-assisted population inversion for Er^{3+} in ZnSe nanosheets, which increases the population of the $^2H_{11/2}$ state as the temperature rises to 298 K.[33,34]

Additionally, double natural logarithm (ln-ln) curves showing the emission intensity and pump power are used to investigate the number of absorbed photons. The emission intensity (I) and pump power (P) obey the relation as $I \propto P^n$, where n represents the number of photons in the luminescence process. For the spectra measured at 77 K, the slopes of green and red emission lines are around 1.31±0.05 and 1.34±0.03, respectively (Figure S14). At 298 K, the slopes (Figure S15) increase to about 1.72±0.04 and 1.83±0.06 for green and red emission bands, respectively. Both the results indicate that a two-photon luminescence process is occurred in the sample under 980 nm excitation. The slope values of green and red emissions at 77 K are lower than those at room temperature; this can be attributed to a higher transition probability of Er^{3+} ions under cryogenic conditions. The decay curves under 980 nm excitation are shown in Figure 4c. At room temperature, the PL decay of Er^{3+} ions in ZnSe nanosheets manifests in emission peaks located at 547.3 and 656.1 nm. After a fitting calculation, the fluorescent lifetimes are determined to be 8.1 and 75.1 μs, respectively, which are similar with the results of Er^{3+} in Yb/Er codoped 2D metal-organic frameworks.[35]

The intrinsic PL spectra of ZnSe nanosheets (shown in Figure 4d) are also investigated at different temperatures under 365 nm excitation. As shown in Figure 4e (middle), these images appear yellow at 77 K, evolving to a weak white color at room temperature. The observed yellow color can be attributed to the defect luminescence from the ZnSe host. The emission peaks are marked as I_1 to I_3 as shown in Figure 4d, which mainly originate from the defect level transitions of ZnSe nanosheets derived from, for instance, Zn-vacancies, stacking faults, and dislocations.[36,37] Among them, the I_3 presents the strongest emission intensity which largely accounts for the yellow luminescence. The intensities from all defect emissions become weaker as the measured temperature increases. The intrinsic emission peak of the ZnSe host is determined to be

I_0 (419 nm), corresponding to 2.96 eV. According to an earlier report, the bandgap of bulk ZnSe was confirmed at around 2.66 eV (466 nm).[38] There is a distinct blue shift compared with the bulk form, which can be attributed to quantum confinement effects in low-dimensional materials.[39] In addition, the CIE chromaticity coordinates are also marked at the inset (left top) of Figure 4d. The specific CIE values are provided at the Figure S16.

Owing to the different thermal response for luminescence of the ZnSe:Er^{3+} nanosheets, the prepared composite film exhibits an interesting color change from 77 K to 298 K. As shown in Figure 4e (top and down), the composite film displays a green color at 77 K and gradually turns to red as the temperature increases. This interesting temperature-dependent luminescence could find promising applications in temperature sensing.
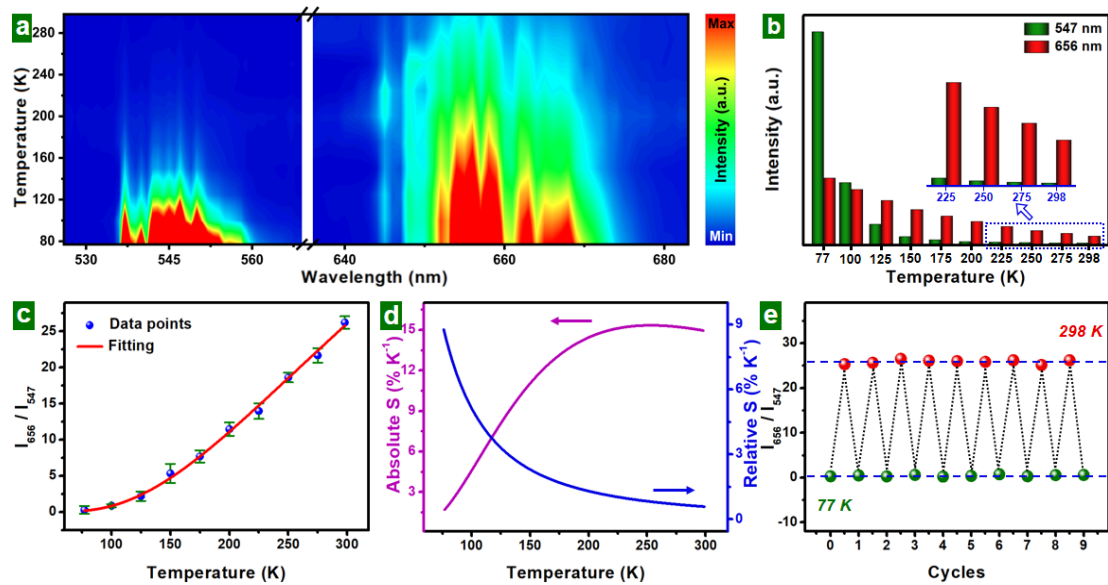
Figure 5. Temperature sensing properties of the ZnSe:Er^{3+} composite film. (a) The contour plot with the color-filling of temperature-dependent emission spectra under 980 nm excitation. (b) Histograms show the emission intensity at 547 and 656 nm at various temperatures. (c) The emission intensity ratio from red to green and corresponding fitted curves. (d) The absolute (left) and relative (right) sensitivity in the range of 77 to 298 K. (e) The repeatability test of the emission intensity ratio (I_{656}/I_{547}) recorded at 77 and 298 K over several cycles.

14

The temperature sensing properties of the ZnSe:Er^{3+} nanosheets are presented in Figure 5. In order to better illustrate the temperature-dependency of the emission, a contour plot is depicted in Figure 5a, with the emission wavelength and temperature on the horizontal and vertical axes, respectively, and the color-filling denoting the emission intensity at each point. In general, the emission intensities of the green and red peaks show a decreasing trend as the temperature increases (Figure S17). This intensity change can be understood by considering the electron-phonon interaction as the temperature varies. According to previous studies, the relationship between the luminescent intensity (I_i) and absolute temperature (T) can be written as follows:[40,41]

$$I_i = N_i R_i \tau = N_i(T) R_i \tau \tag{1}$$

$$\frac{1}{\tau} = R + W_{NR} \tag{2}$$

$$W_{NR}(T) = W_{NR}(0)[1 - \exp\left(-\frac{\hbar\omega}{K_B T}\right)]^{-P} \tag{3}$$

where $N(T)$ denotes the excited states' population at a certain temperature T, τ is the lifetime for excited states, P denotes the phonons number, $\hbar\omega$ is the energy of the phonons, and R and W_{NR} represent the radiative and non-radiative transition rate, respectively. After combining equations 1 to 3, the intensity is explicitly expressed as:[41]

$$I_i = N_{i,\infty}[\exp\left(-\frac{p_i \Delta E}{K_B T}\right)][\exp\left(-\frac{K_B T}{E_q}\right)]^{P_i}$$

$$\{1 - \tau W_{NR}(0)[1 - \exp\left(-\frac{\hbar\omega}{K_B T}\right)]^{-P}\} \tag{4}$$

Here, ΔE is the energy gap between the excited and ground states. It can be clearly noted from equation 4 that the emission intensity is mainly affected by two processes: non-radiative decay and thermal agitation. Consequently, under a low-temperature environment, the non-radiative rate is at an extremely low level while the rate of thermal distribution is relatively high. This results in stronger emission intensity at lower temperature. However, at high-temperature range, it suggests a rapid increase for the non-radiative rate and leads to a decline in the radiation probability, which eventually brings about an emission intensity

decrease. Besides this, there is a clearly observable difference in temperature-dependence between the two emission peaks, where the green emission shows a stronger thermal quenching. This result can largely be attributed to the non-radiative decay, thermal agitation and quenching activation energy. Since the photon energy at 547 nm is considerably higher than the photon at 656 nm. According to equation 1-4, the non-radiative decay, thermal agitation and quenching activation energy at 547 nm is more significant. Therefore, the emission intensity at 547 nm is reduced more strongly as the temperature increases. This phenomena brings about an abundant color change from green (0.32, 0.67) to red (0.64, 0.36) in CIE chromaticity coordinates (Figure S18).

Further to this, the emission peaks located at 547 nm (green) and 656 nm (red) are analyzed with respect to their use in optical thermometry. As shown in Figure 5b, the specific thermal quenching trend of the two emission peaks at 547 and 656 nm is marked and described. It is seen that the emission intensity at 547 nm tends to decline rapidly as the temperature increases. Meanwhile, the emission intensity decreases more gradually for the peak at 656 nm. As aforementioned, the non-radiative decay, thermal agitation and quenching activation energy lead to the different thermal quenching performance of the two emission peaks at 547 and 656 nm. This thermal quenching could present ZnSe:Er^{3+} nanosheets as a viable solution for optical thermometry applications.

As depicted in Figure 5c, the thermometric parameter LR is defined as the luminescence intensity ratio between the green (547 nm) and red (656 nm) emission. The parameter LR reveals an exponential relationship with the temperature from 77 to 298 K, which can be expressed as the equation 5.[42]

$$LR \equiv \frac{I_{656}}{I_{547}} = C_1 \cdot \exp\left(\frac{-C_2}{T}\right) \tag{5}$$

where C_1, C_2 represent the constants and T denotes the absolute temperature. The fitted curve can be specifically described as $LR = 143.93\exp(-512.20/T)$. The fitting value of R^2 is 0.9989. In addition, the two indices of absolute and relative sensitivity (S_a and S_r) are of great importance for assessing the optical thermometry property as

described in equation 6 and 7.[43]

$$S_a = \frac{\partial LR}{\partial T} = LR \cdot \left(\frac{C_2}{T^2}\right) \tag{6}$$

$$S_r = \frac{1}{LR} \cdot \frac{\partial LR}{\partial T} = \frac{C_2}{T^2} \tag{7}$$

As shown in Figure 5d, the maximal value of absolute thermal sensitivity S_a is 15.23% K^{-1} at 250 K. The maximum value of relative sensitivity S_r is determined to be 8.61% K^{-1} at 77 K (Figure S19, S20). These results for S_a and S_r are superior to conventional Er^{3+} activated upconversion luminescent nanothermometer reported thus far (Table S4). It is deduced that 2D nanosheets possess some advantages over the systems previously reported, including high specific surface area, an abundance of active sites, as well as in their optical carrier transport, and quantum confinement effects.[4,44,45] Furthermore, the 2D nanosheets present a different phonon vibration mode compared with other bulk crystals and nanomaterials. Moreover, the temperature resolution of the prepared nanosheets is determined to be lower than 0.8 K over the total temperature range, and better than 0.5 K (Figure S21) under the temperature of 250 K.

Performance stability is vital for practical applications in temperature sensing. Therefore, reproductivity tests were also implemented, under 980 nm excitation. As shown in Figure 5e and S22, the thermometric parameter LR (I_{656}/I_{547}) is maintained at almost the same level over 9 cycles of heating and cooling from 77 to 298 K, establishing a lower bound for their stability and reliability. Further studies would be required to assess the long-term stability of operation.

CONCLUSIONS

In summary, Er^{3+} ions doped 2D ZnSe nanosheets have been fabricated. Investigations into their structure and morphology using TEM, HR-TEM, CS-STEM, AFM, Raman, EDS and XPS demonstrate that the Er^{3+} ions have been introduced into the ultrathin layered ZnSe host. Low temperature (4 K) UC and DC PL fine spectra of Er^{3+} ions were measured under the 980 nm diode laser excitation, indicating a total number of fifty-one CF lines from the UV to NIR emission range. The acquired UV spectra of Er^{3+} ions imply that the luminescent

properties of RE ions in 2D nanomaterials could overcome the bandgap limitations of conventional 2D semiconductor hosts. Notably, the prepared PDMS composite film exhibits a diversity of color variation from 77 K to room temperature. Under NIR (980 nm) and UV (365 nm) excitations, the color changes can be obviously observed from green to red, and yellow to weak white, respectively. Furthermore, the Er^{3+} ions with separated sublevel transitions at 547.3 and 656.1 nm show different thermal quenching effects, which could be employed for optical thermometry. After fitting calculations, the obtained maximal values of S_a and S_r are determined to be 15.23% and 8.61% K^{-1}, respectively. Taking advantages of the direct wide-bandgap ZnSe semiconductor and enriched energy levels for RE ion dopants, our work realizes multi-color luminescence and excellent temperature sensing performance, inspiring promising applications in 2D functional nanodevices.

MATERIALS AND METHODS

Chemicals and Materials. The raw materials ZnSe (99.99%) were purchased from Aladdin Industrial Corporation; ErF_3 powders (99.99%) were acquired from Sinopharm Chemical Reagent Corporation. The analytical reagent ethanol was bought from Hangzhou Gaojing Fine Chemical Industry Corporation.

Sample preparation. The Er^{3+} doped ZnSe nanosheets were prepared by two steps. First, the Er^{3+} doped ZnSe powders were mixed and ground according to the formula of $Zn_{0.99}Er_{0.01}Se$ (Figure S23). Then the mixtures were sintered with supplementary Se at 950 ℃ for 4 hrs in Ar gas. Secondly, the ZnSe:Er^{3+} nanosheets were gained through liquid phase exfoliation process. In detail, the grinded ZnSe:Er^{3+} powders (50 mg) were dispersed in 100 ml ethanol. Next, the bulk solution with concentration 0.5 g/L was exfoliated by ultrasonic machine for 48 hrs under 10 ℃. Finally, the ZnSe:Er^{3+} nanosheets were collected from supernatant with concentration 0.1 g/L by centrifugation in 6000 r/min for 10 mins.

Characterization. The Bruker XRD instrument (D2 PHASER, Germany) equipped with Cu Kα radiation was served for the crystal phase. The micromorphology was

observed by Tecnai FEI TEM (G2 F20, USA) and Hitachi SEM (SU8010, Japan). The thickness information was gained from Dimensional AFM (Veeco, Nanoscope V, USA) using tap mode. The atomic-resolution STEM was performed in a JEOL ARM200F with STEM aberration (Cs) corrector operated at 80 kV. The Renishaw Raman spectrograph (inVia-Reflex, UK) was used to acquire the microstructure data with a 532 nm laser. The existed elements of as-prepared nanosheets were detected by Thermo Fisher XPS (Escalab 250Xi, USA) equipped with Al Kα source (hν = 1361 eV). The element distribution of ZnSe:Er^{3+} sample was collected by EDS with Oxford Instruments XMaxN 100TLE 100 mm^2 detector. The emission spectra were monitored via fluorescence spectrometer (FL3, Jobin Yvon, France), equipped with Xe lamp and a 980 nm laser. In particular, the ZnSe:Er^{3+} nanosheets were dropped in sample holder for 4 K fine emission spectra. The specific parameters include 0.1 nm step size, 0.1 nm side entrance and exit slit, 0.2 s integration time, 1200 grating, and pump power of 0.4 W in continuous wave mode. On the other hand, the prepared nanosheets were dispersed in PDMS for the temperature dependent emission spectra. The measuring parameters include 1 nm step size, 1 nm side entrance and exit slit, 0.1 s integration time, 1200 grating, and 1 W pump power in continuous wave mode. The PL decay curves were recorded on HORIBA (QM 8075-11, Canada) spectrofluorometer. In details, the test parameters include 1 nm entrance and exit slit, 1000 μs end time, 1000 acquisition points, and 2 W pump power in impulse wave mode. The absorbance spectra were collected by a UV3600 spectrophotometer (Shimadzu Corporation, Kyoto, Japan) equipment with an integrating sphere. The temperature control system (OpistatAc-V12A, UK) was used to measure the temperature dependent emission spectra.

ASSOCIATED CONTENT

Supporting Information

The Supporting Information is available free of charge on the ACS Publications website at DOI: XX/XX.

The crystal structure information of ZnSe host; The sub-level transitions of ZnSe:Er^{3+} nanosheets at 4 K; The table of The 4 K fine emission peaks; Table of typical Er^{3+}-activated temperature sensing materials; The XRD patterns and SEM images; The structural models; The EDS images; The emission spectra of ZnSe:Er^{3+} bulk powder and nanosheets; The absorbance spectra and temperature dependent emission spectra of ZnSe:Er^{3+} bulk powder and nanosheets. (PDF)

AUTHOR INFORMATION

Corresponding Author

*E-mail (G. Bai): baigx@cjlu.edu.cn.

*E-mail (S. Xu): shiqingxu@cjlu.edu.cn

*E-mail (J. Hao): jh.hao@polyu.edu.hk

Notes

There are no conflicts to declare.

REFERENCES

(1) Gibertini, M.; Koperski, M.; Morpurgo, A. F.; Novoselov, K. S. Magnetic 2D Materials and Heterostructures. *Nat. Nanotechnol.* **2019**, *14*, 408-419.

(2) He, Q.; Zhang, H. Electrically Detecting Infrared Light. *Nat. Mater.* **2018**, *17*, 950-951.

(3) Dai, Z.; Liu, L.; Zhang, Z. Strain Engineering of 2D Materials: Issues and Opportunities at the Interface. *Adv. Mater.* **2019**, *31*, 1805417.

(4) Tan, C.; Cao, X.; Wu, X.; He, Q.; Yang, J.; Zhang, X.; Chen, J.; Zhao, W.; Han, S.; Nam, G.-H.; Sindoro, M.; Zhang, H. Recent Advances in Ultrathin Two-Dimensional Nanomaterials. *Chem. Rev.* **2017**, *117*, 6225-6331.

(5) Desai, S. B.; Madhvapathy, S. R.; Sachid, A. B.; Llinas, J. P.; Wang, Q.; Ahn, G. H.; Pitner, G.; Kim, M. J.; Bokor, J.; Hu, C. MoS_2 Transistors with 1-Nanometer Gate Lengths. *Science* **2016**, *354*, 99-102.

(6) Zhou, B.; Yan, D. Simultaneous Long-Persistent Blue Luminescence and High Quantum Yield within 2D Organic-Metal Halide Perovskite Micro/Nanosheets. *Angew. Chem. Int. Ed.* **2019**, *58*, 15128-15135.

(7) Dhakshinamoorthy, A.; Asiri, A. M.; Garcia, H. 2D Metal-Organic Frameworks as Multifunctional Materials in Heterogeneous Catalysis and Electro/Photocatalysis. *Adv. Mater.* **2019**, *31*, 1900617.

(8) Das, S.; Pandey, D.; Thomas, J.; Roy, T. The Role of Graphene and Other 2D Materials in Solar Photovoltaics. *Adv. Mater.* **2019**, *31*, 1802722.

(9) Wu, Y.; Xu, J.; Poh, E. T.; Liang, L.; Liu, H.; Yang, J.; Qiu, C.-W.; Vallée, R.; Liu, X. Upconversion Superburst with Sub-2 μs Lifetime. *Nat. Nanotechnol.* **2019**, *14*, 1110-1115.

(10) Zhou, J.; Wen, S.; Liao, J.; Clarke, C.; Tawfik, S. A.; Ren, W.; Mi, C.; Wang, F.; Jin, D. Activation of the Surface Dark-Layer to Enhance Upconversion in a Thermal Field. *Nat. Photon.* **2018**, *12*, 154-158.

(11) Su, L.; Fan, X.; Yin, T.; Wang, H.; Li, Y.; Liu, F.; Li, J.; Zhang, H.; Xie, H. Inorganic 2D Luminescent Materials: Structure, Luminescence Modulation, and Applications. *Adv. Opt. Mater.* **2019**, *8*, 1900978.

(12) Zhang, J.; Yu, Y.; Wang, P.; Luo, C.; Wu, X.; Sun, Z.; Wang, J.; Hu, W. D.; Shen, G. Characterization of Atomic Defects on the Photoluminescence in Two-Dimensional Materials Using Transmission Electron Microscope. *InfoMat.* **2019**, *1*, 85-97.

(13) Chiu, M. H.; Tang, H. L.; Tseng, C. C.; Han, Y.; Aljarb, A.; Huang, J. K.; Wan, Y.; Fu, J. H.; Zhang, X.; Chang, W. H.; Muller, D. A.; Takenobu, T.; Tung, V.; Li, L. J. Metal-Guided Selective Growth of 2D Materials: Demonstration of a Bottom-Up

CMOS Inverter. *Adv. Mater.* **2019**, *31*, 1900861.

(14) Hennighausen, Z.; Bilgin, I.; Casey, C.; Kar, S. Widely Tunable Bi_2Se_3/Transition Metal Dichalcogenide 2D Heterostructures for Write-Read-Erase-Reuse Applications. *2D Mater.* **2019**, *6*, 041003.

(15) Zhao, Y.; Yu, D.; Lu, J.; Tao, L.; Chen, Z.; Yang, Y.; Wei, A.; Tao, L.; Liu, J.; Zheng, Z.; Hao, M.; Xu, J. B. Thickness-Dependent Optical Properties and In-Plane Anisotropic Raman Response of the 2D β-In_2S_3. *Adv. Opt. Mater.* **2019**, *7*, 1901085.

(16) Li, X.-L.; Han, W.-P.; Wu, J.-B.; Qiao, X.-F.; Zhang, J.; Tan, P.-H. Layer-Number Dependent Optical Properties of 2D Materials and Their Application for Thickness Determination. *Adv. Funct. Mater.* **2017**, *27*, 1604468.

(17) Hu, G.; Ou, Q.; Si, G.; Wu, Y.; Wu, J.; Dai, Z.; Krasnok, A.; Mazor, Y.; Zhang, Q.; Bao, Q.; Qiu, C. W.; Alu, A. Topological Polaritons and Photonic Magic Angles in Twisted Alpha-MoO_3 Bilayers. *Nature* **2020**, *582*, 209-213.

(18) Zhang, K.; Feng, S.; Wang, J.; Azcatl, A.; Lu, N.; Addou, R.; Wang, N.; Zhou, C.; Lerach, J.; Bojan, V.; Kim, M. J.; Chen, L. Q.; Wallace, R. M.; Terrones, M.; Zhu, J.; Robinson, J. A. Manganese Doping of Monolayer MoS_2: The Substrate Is Critical. *Nano Lett.* **2015**, *15*, 6586-6591.

(19) Lin, Y. C.; Dumcenco, D. O.; Komsa, H. P.; Niimi, Y.; Krasheninnikov, A. V.; Huang, Y. S.; Suenaga, K. Properties of Individual Dopant Atoms in Single-Layer MoS_2: Atomic Structure, Migration, and Enhanced Reactivity. *Adv. Mater.* **2014**, *26*, 2857-2861.

(20) Bai, G.; Yuan, S.; Zhao, Y.; Yang, Z.; Choi, S. Y.; Chai, Y.; Yu, S. F.; Lau, S. P.; Hao, J. 2D Layered Materials of Rare-Earth Er-Doped MoS_2 with NIR-to-NIR Down- and Up-Conversion Photoluminescence. *Adv. Mater.* **2016**, *28*, 7472-7477.

(21) Sun, Y.; Sun, Z.; Gao, S.; Cheng, H.; Liu, Q.; Piao, J.; Yao, T.; Wu, C.; Hu, S.; Wei, S.; Xie, Y. Fabrication of Flexible and Freestanding Zinc Chalcogenide Single Layers. *Nat. Commun.* **2012**, *3*, 1057.

(22) Yu, S.; Tu, D.; Lian, W.; Xu, J.; Chen, X. Lanthanide-Doped Near-Infrared II Luminescent Nanoprobes for Bioapplications. *Sci. China Mater.* **2019**, *62*, 1071-1086.

(23) Piñol, R.; Zeler, J.; Brites, C. D. S.; Gu, Y.; Téllez, P.; Carneiro Neto, A. N.; da Silva, T. E.; Moreno-Loshuertos, R.; Fernandez-Silva, P.; Gallego, A. I.; Martinez-Lostao, L.; Martínez, A.; Carlos, L. D.; Millán, A. Real-Time Intracellular Temperature Imaging Using Lanthanide-Bearing Polymeric Micelles. *Nano Lett.* **2020**, *20*, 6466-6472.

(24) Yu, S.; Xu, J.; Shang, X.; Zheng, W.; Huang, P.; Li, R.; Tu, D.; Chen, X. A Dual-Excitation Decoding Strategy Based on NIR Hybrid Nanocomposites for High-Accuracy Thermal Sensing. *Adv. Sci.* **2020**, *7*, 2001589.

(25) Kaczmarek, A. M.; Liu, Y. Y.; Kaczmarek, M. K.; Liu, H.; Artizzu, F.; Carlos, L. D.; Van Der Voort. P. Developing Luminescent Ratiometric Thermometers Based on a Covalent Organic Framework (COF). *Angew. Chem. Int. Ed.* **2020**, *59*, 1932-1940.

(26) Chen, D.; Wan, Z.; Zhou, Y.; Zhou, X.; Yu, Y.; Zhong, J.; Ding, M.; Ji, Z. Dual-Phase Glass Ceramic: Structure, Dual-Modal Luminescence and Temperature Sensing Behaviors. *ACS Appl. Mater. Inter.* **2015**, *7*, 19484-19493.

(27) Guo, J.; Zhou, B.; Yang, C.; Dai, Q.; Kong, L. Stretchable and Temperature-Sensitive Polymer Optical Fibers for Wearable Health Monitoring. *Adv. Funct. Mater.* **2019**, *29*, 1902898.

(28) Lüth, H. Solid Surfaces, Interfaces and Thin Films. *Springer*, Berlin, **2001**, Vol.4.

(29) Xiong, S.; Xi, B.; Wang, C.; Xi, G.; Liu, X.; Qian, Y. Solution-Phase Synthesis and High Photocatalytic Activity of Wurtzite ZnSe Ultrathin Nanobelts: A General Route to 1D Semiconductor Nanostructured Materials. *Chem. Eur. J.* **2007**, *13*, 7926, 1902898.

(30) Nada, K. K.; Sarangi, S. N.; Sahu, S. N.; Deb, S. K.; Behera, S. N. Raman Spectroscopy of CdS Nanocrystalline Semiconductors. *Physica B* **1999**, *262*, 31-39.

(31) Kwon, B.-H.; Jang, H. S.; Yoo, H. S.; Kim, S. W.; Kang, D. S.; Maeng, S.; Jang, D. S.; Kim, H.; Jeon, D. Y. White-Light Emitting Surface-Functionalized ZnSe Quantum Dots: Europium Complex-Capped Hybrid Nanocrystal. *J. Mater. Chem.* **2011**, *21*, 12812-12818.

(32) Jaramillo, T. F.; Jørgensen, K. P.; Bonde, J.; Nielsen, J. H.; Horch, S.; Chorkendorff, I. Identification of Active Edge Sites for Electrochemical H_2 Evolution from MoS_2 Nanocatalysts. *Science* **2007**, *317*, 100-102.

(33) Zhang, Q.; Liu, X.; Utama, M. I.; Xing, G.; Sum, T. C.; Xiong, Q. Phonon-Assisted Anti-Stokes Lasing in ZnTe Nanoribbons. *Adv. Mater.* **2016**, *28*, 276-283.

(34) Xu, X.; Zhang, W.; Yang, D.; Lu, W.; Qiu, J.; Yu, S. F. Phonon-Assisted Population Inversion in Lanthanide-Doped Upconversion Ba_2LaF_7 Nanocrystals in Glass-Ceramics. *Adv. Mater.* **2016**, *28*, 8045-8050.

(35) Artizzu, F.; Atzori, M.; Liu, J.; Mara, D.; Van Hecke, K.; Van Deun, R. Solution-Processable Yb/Er 2D-Layered Metallorganic Frameworks with High NIR-Emission Quantum Yields. *J. Mater. Chem. C* **2019**, *7*, 11207-11214.

(36) Dey, S. C.; Nath, S. S. Electroluminescence of Colloidal ZnSe Quantum Dots. *J. Lumin.* **2011**, *131,* 2707-2710.

(37) Fujita, S.; Mimoto, H.; Noguchi, T. Photoluminescence in ZnSe Grown by Liquid-Phase Epitaxy from Zn-Ga Solution. *J. Appl. Phys.* **1979**, *50*, 1079-1087.

(38) Tian, L.; di Mario, L.; Zannier, V.; Catone, D.; Colonna, S.; O'Keeffe, P.; Turchini, S.; Zema, N.; Rubini, S.; Martelli, F. Ultrafast Carrier Dynamics, Band-Gap Renormalization, and Optical Properties of ZnSe Nanowires. *Phys. Rew. B* **2016**, *94*, 165442.

(39) Heulings, H. R. I.; Huang, X.; Li, J. Mn-Substituted Inorganic-Organic Hybrid Materials Based on ZnSe: Nanostructures That May Lead to Magnetic Semiconductors with a Strong Quantum Confinement Effect. *Nano Lett.* **2001**, *1*, 521-525.

(40) Wu, K.; Cui, J.; Kong, X.; Wang, Y. Temperature Dependent Upconversion Luminescence of Yb/Er Codoped $NaYF_4$ Nanocrystals. *J. Appl. Phys.* **2011**, *110*, 053510.

(41) Bai, G.; Tsang, M.-K.; Hao, J. Tuning the Luminesence of Phosphors: Beyond Conventional Chemical Method. *Adv. Opt. Mater.* **2015**, *3*, 431-462.

(42) Zou, H.; Yang, X.; Chen, B.; Du, Y.; Ren, B.; Sun, X.; Qiao, X.; Zhang, Q.; Wang, F. Thermal Enhancement of Upconversion by Negative Lattice Expansion in

Orthorhombic $Yb_2W_3O_{12}$. *Angew. Chem. Int. Ed.* **2019**, *58*, 17255-17259.

(43) Huang, P.; Zheng, W.; Tu, D.; Shang, X.; Zhang, M.; Li, R.; Xu, J.; Liu, Y.; Chen, X. Unraveling the Electronic Structures of Neodymium in $LiLuF_4$ Nanocrystals for Ratiometric Temperature Sensing. *Adv. Sci.* **2019**, *6*, 1802282.

(44) Cheng, L.; Wang, X.; Gong, F.; Liu, T.; Liu, Z. 2D Nanomaterials for Cancer Theranostic Applications. *Adv. Mater.* **2019**, *32*, 1902333.

(45) Tan, C.; Lai, Z.; Zhang, H. Ultrathin Two-Demensional Multinary Layered Metal Chalcogenide Nanomaterials. *Adv. Mater*. **2017**, *29*, 1701392.

Table of Contents Image